

A 2-Dimensional Generalized Likelihood Ratio Test for Land Mine and Small Unexploded Ordnance Detection

Ping Gao and Leslie M. Collins

Abstract

The fundamental goals of land-mine and small unexploded ordnance (UXO) detection are to achieve a high probability of detection (P_d) and a low probability of false alarm (P_{fa}). Conventional methods usually fulfill the first goal at the cost of a high P_{fa} . In our previous work [1], [2], [3], we have shown that a Bayesian decision theoretic approach can be applied to improve the detectability of land mines and small UXO targets using a single spatial sample of the electromagnetic induction (EMI) sensor data. In this paper, we present an alternative approach which significantly improves P_d at a fixed P_{fa} by utilizing features that capture the physical nature of EMI data within a statistical signal processing framework. The method we develop is a two-dimensional generalized likelihood ratio test (2-D GLRT) which utilizes spatial information from the sensor output. To illustrate the performance improvement, results obtained with the 2-D GLRT detector are compared to those for the standard threshold test for single channel time-domain sensor data, as well as the energy detector, the integral detector, and the single location generalized likelihood ratio test (1-D GLRT) detector for multi-channel time-domain EMI sensor data.

Keywords

Detection theory, Electromagnetic induction, Land mine detection, UXO detection.

P. Gao and L. Collins are members of the Electrical and Computer Engineering Department, Duke University, Durham, NC 27708-0291, U.S.A. Telephone: 919-660-5260, Fax: 919-660-5293, E-mail: pgao@ee.duke.edu, lcollins@ee.duke.edu.

Special symbols used in this paper

ω_n

$\alpha, \alpha_1, \alpha_0, \beta$

σ^2, δ

$r, \underline{S}_1, \underline{S}_0, \hat{S}_1, \hat{S}_0$

λ

Π_i

$\underline{\mu}_{d_1}, \underline{\mu}_{d_0}, \underline{\mu}_{y_1}, \underline{\mu}_{y_0}$

$\underline{\Sigma}_{d_1}, \underline{\Sigma}_{d_0}, \underline{\Sigma}_{y_1}, \underline{\Sigma}_{y_0}$

$\hat{\underline{\mu}}_{d_1}$ and $\hat{\underline{\mu}}_{d_0}$

$\hat{\underline{\Sigma}}_{d_1}, \hat{\underline{\Sigma}}_{d_0}, \hat{\underline{\Sigma}}_{y_1},$ and $\hat{\underline{\Sigma}}_{y_0}$

The paper contains total of 44 pages, 4 tables, 13 figures.

I. INTRODUCTION

The goal of any detection system is to achieve a high probability of detection (P_d) while at the same time maintaining a low probability of false alarm (P_{fa}). This is particularly important in land mine detection where P_d is required by the United Nations to be 99.6%, and P_{fa} is directly proportional to the time and cost to remediate a site. At the current rate of clearance, 1,100 years will be required to remove all land mines that are already emplaced (This statistic further assumes that no additional land mines are emplaced.) Thus, reducing the false alarm rate is of immediate importance. However, it is most often the case that land mine detectors which achieve high P_d do so at the cost of high P_{fa} . This is because conventional mine detection technologies simply seek anomalies caused either by land mines or clutter, but do not exploit the nature of the physical signature or the statistics of the sensor response due to mines and clutter. In this paper, we present an approach which significantly reduces P_{fa} at a fixed P_d by incorporating the underlying physics of electromagnetic induction (EMI) sensors into a statistical signal processing framework. This novel method is a two-dimensional generalized likelihood ratio test (2-D GLRT) algorithm, which utilizes the spatial measurements taken with an EMI sensor across a local area.

There are several devices which either have been used or have been proposed for use in land mine detection: magnetometer, infrared imager, electromagnetic induction (EMI) sensor, and ground penetrating radar (GPR). Among these sensors, the most well established is the EMI sensor. An EMI system is essentially a metal sensor which records the electromagnetic induction field that is the response from underground objects, clutter, etc. due to an incident electromagnetic field. An EMI system can detect mines which contain metal, as well as unexploded ordnance (UXO) or metallic anthropic clutter. In order to detect such targets, the EMI system normally operates at low frequencies ($< 1\text{MHz}$), at which the conductivity- and permeability-dependent skin depth of the materials varies significantly [4], [12]. Furthermore, at these frequencies the displacement current is weak enough to be neglected [6]. Hence, the response of the pulsed EMI system, \mathbf{r} , at each location surveyed with the sensor can be modeled as a superposition of weighted resonant

responses:

$$\mathbf{r} = \sum_{n=1}^N A_n e^{-j\omega_n t} \quad (1)$$

where ω_n is the n -th natural resonant frequency of the object and A_n is the initial magnitude of the response corresponding to that natural resonant frequency. In practice, the real part of ω_n is very small, and thus can be ignored [6]. Also, the late time field, which is the field recorded by EMI sensors, is dominated by the lowest mode, which is approximately an exponential damping. Therefore, to a first order approximation the response can be modeled as:

$$\mathbf{r} = A e^{-\alpha t} \quad (2)$$

where A is the initial magnitude of the response and α is the dominant natural resonant frequency. A is strongly dependent on the excitation level, the depth, and the orientation of the underground objects [6], [12]. The resonant frequency, α , can be used to identify land mines because it is a function of conductivity and permeability, which are unique to each metal type [4], [12], [6]. Generally, the response from a relatively high metal content mine has a lower natural resonant frequency than that of anthropic clutter, *i.e.* the decay rate of a target signature is slower.

In this paper, several detection approaches are explored for two types of EMI sensors: (1) multi-channel time-domain EMI systems and (2) single channel integrated time-domain EMI systems. The detection approaches are validated using field data collected in conjunction with the *DARPA Backgrounds Clutter Data Collection Experiment* [7]. One example of a prototype multi-channel time-domain pulsed EMI sensor is the Geonics EM61-3D sensor, which was used to collect data in the *DARPA* experiment. This sensor samples the induced response at 20 geometrically spaced time gates from $320\mu s$ to $30ms$ following the incident pulse [7]. Thus, the received signal from the Geonics EM61-3D sensor can be expressed as:

$$\underline{\mathbf{r}} = A e^{-\alpha \underline{t}} \quad (3)$$

where $\{t_i\}$, an element of \underline{t} , is the sampling time, $i = 1, 2, \dots, 20$. An example of the second type of sensors, a single channel time-domain EMI system, is the Geonics EM61 sensor, also used in the *DARPA* study. This sensor integrates the time-domain induced response

within a pre-determined range of time to obtain a scalar value at each survey location. Therefore, its response can be expressed approximately as:

$$\mathbf{r} = \sum_{i=0}^N A e^{-\alpha(t_0+i\Delta t)} \quad (4)$$

where t_0 is the initial time for the integration, and the integration ends at time $t_0 + N\Delta t$.

The traditional approach to mine detection using data from a single channel EMI sensor is to perform a threshold test on the data obtained at each individual survey location. As stated before, the phenomenon exploited to distinguish mines from clutter is that the decay rate of the target response is generally slower than that of clutter. Discrimination based on the initial magnitude A is not investigated in this paper; however, experimental data indicates that, on average, A for mines is greater than that of clutter. Thus, after integrating the response, the output from a single channel integrated time-domain EMI sensor due to a target is usually greater than that of clutter. An extension of this approach to multi-channel EMI sensor data is to perform a threshold test on either the energy present in the received signal, or on the integral (sum) of the sampled values at each survey location. These two approaches essentially convert the multi-channel responses to single channel data in order to make a decision.

In addition to the conventional methods, there have been several studies on mine detection using statistical methods. In [1], [2], [3], [8], [9], [10], the statistical characterization and modeling of mine fields have been addressed. Reference [11] introduced an area-based “ δ -technique”, which incorporates spatial information through the energy levels of an EMI sensor response at the center point under test and its immediate neighbors. This technique utilizes the number of neighbors whose energy level is lower than that of the center location under test as the criterion of whether a mine is present or not. This technique is similar to CFAR detection [18].

In our previous work [1], [2], [3], we have applied signal detection theory to generate both the one-dimensional likelihood ratio test (LRT) and the GLRT for the Geonics EM61 and EM61-3D sensor data. The probability density functions describing the sensor response

to target and clutter were used to formulate the likelihood ratio at each surveyed location. We have shown that the performance of the two detection approaches were the same experimentally and theoretically for multi-channel sensor data [3], [17]. In addition, the 1-D GLRT has been shown to improve performance dramatically over the performance achieved with the standard tests on multi-channel sensor data. We have also proven that a threshold test on the raw data is the optimal processor for single channel EMI sensor data from a single location, even when the decay rates for target and clutter are not deterministic parameters [1].

In this paper, a statistical approach incorporating both the underlying physics of EMI sensors [4], [5], [12], [13], [14] and statistical signal processing theory [15], in which the statistics of local data surrounding the location under test are utilized, is presented. Since the minefields are sampled spatially, *i.e.* the sensor head is moved throughout the candidate area, we have hypothesized that the accuracy of the mine detectors would be improved when spatial information is incorporated into processor. The results demonstrate that this hypothesis is valid.

The remainder of this paper is organized as follows. In order to illustrate the improvement of the 2-D GLRT, it is compared to several other detection schemes including the threshold, energy, and integral detectors, the δ -technique, and the 1-D GLRT. Each of these detectors is described in Sec. II. In Sec. III we introduce a 2-dimensional GLRT detector for land mine and small UXO detection. The field data utilized to analyze performance is described in Sec. IV. Next, the results obtained by applying each of these detectors to the experimental data are presented in Sec. V. Finally, the results are discussed in Sec. VI.

II. 1-DIMENSIONAL GENERALIZED LIKELIHOOD RATIO TEST AND OTHER DETECTORS

First, several simple detection approaches are described. It is necessary to investigate these detection techniques in order to evaluate the significance of the performance im-

provement achieved by the 2-D GLRT. The distributions of the outputs of multi-channel time-domain EMI sensors can be modeled with multivariate Gaussian density functions [1]. $\underline{r}|H_1 \sim \mathcal{N}(\underline{S}_1(A_1, \alpha_1), \sigma^2 I)$ and $\underline{r}|H_0 \sim \mathcal{N}(\underline{S}_0(A_0, \alpha_0), \sigma^2 I)$ where \underline{r} is the output of the sensor as a function of time, A_1 and A_0 are the initial magnitude and α_1 and α_0 are the natural resonant frequencies under H_1 (target-present hypothesis) and H_0 (no-target) hypothesis, $\underline{S}_1(A_1, \alpha_1) = A_1 e^{-\alpha_1 \underline{t}}$, $\underline{S}_0(A_0, \alpha_0) = A_0 e^{-\alpha_0 \underline{t}}$, which correspond to theoretical values of the sensor output of the target and clutter under the parameters of A_1 , α_1 , A_0 , and α_0 at sample time \underline{t} , I is N by N identity matrix where N is 20 for data from the Geonics EM61-3D sensor, and σ^2 is variance of each element of \underline{r} . Since the sensor is assumed to be subject to independent identical Gaussian white noise, the variance of each element of \underline{r} is the same. This hypothesis was verified by examining the field data [1]. Thus, the generalized likelihood ratio test for a single spatial measurement can be formulated [2] as:

$$\lambda(\underline{r}) = \frac{\prod_i e^{-\frac{[r_i - \hat{S}_{1i}(\hat{A}_1, \hat{\alpha}_1)]^2}{2\hat{\sigma}^2}}}{\prod_i e^{-\frac{[r_i - \hat{S}_{0i}(\hat{A}_0, \hat{\alpha}_0)]^2}{2\hat{\sigma}^2}}} \quad (5)$$

where r_i is the output of the sensors at time indices $i = 1, 2, \dots, 20$, and $\hat{\sigma}^2$, $\hat{S}_{1i}(\hat{A}_1, \hat{\alpha}_1)$ and $\hat{S}_{0i}(\hat{A}_0, \hat{\alpha}_0)$ are the maximum likelihood estimates (MLE) of σ^2 , $S_{1i}(A_1, \alpha_1)$ and $S_{0i}(A_0, \alpha_0)$.

Since A_1, α_1, A_0 and α_0 are random variables (rv's), a Least-Squares method was used to estimate A_1, α_1 for each H_1 item and A_0, α_0 for each H_0 item from data taken in the calibration area, an area which provided training data (details can be found in Sec. IV.A). The sample means of these estimates are denoted $\hat{A}_1, \hat{\alpha}_1, \hat{A}_0$, and $\hat{\alpha}_0$, which are the estimates of A_1, α_1, A_0 and α_0 used for Eqn. (5). Thus, $\hat{S}_{1i}(\hat{A}_1, \hat{\alpha}_1) = \hat{A}_1 e^{-\hat{\alpha}_1 t_i}$ and $\hat{S}_{0i}(\hat{A}_0, \hat{\alpha}_0) = \hat{A}_0 e^{-\hat{\alpha}_0 t_i}$. A GLRT was used, as the prior knowledge available from the calibration area regarding the distribution of the random parameters was not considered statistically reliable due to the paucity of emplaced targets in the test sites. (Only 14 metal targets were emplaced in the calibration area and could be used for the estimation of A_1 and α_1 . However, the calibration area contained 886 locations which could be used to estimate A_0 and α_0 .) It should be noted that 1-D GLRT detectors provide processors which in some instances achieve performance that is identical to that of the likelihood ratio test performed at single location [17], although in general they are not optimum [15], [16]. The optimal detector requires integration over all uncertain parameters, and

the computational expense associated with evaluation of the multidimensional integral usually precludes implementing an optimal detector.

The standard threshold test for single channel integrated time-domain EMI data was also implemented for the EM61 sensor, since in this case the single location optimal detector reduces to a threshold detector as shown in [1], [3]. Other standard detectors, such as the energy and integral detectors, were also implemented for the multi-channel time-domain EMI data. The energy detector is essentially a threshold test performed on the energy presented at each surveyed location. The integral detector is a processor which integrates, or sums the time samples at each location to obtain a scalar output and then thresholds the output.

The δ -technique is an approach which includes spatial information into the decision-making process in an ad-hoc fashion [11]. This method simply considers the number of immediate neighbors (up to 8 neighbors in the case of *DARPA* data) whose energy values are strictly less than that of the center location under test as the statistic used to make a mine or no-mine decision. When this number is greater than a pre-determined integer value (usually 7 or 8), the decision made is that a mine is present; otherwise a no-mine decision is made.

III. DETECTOR DESIGN - 2-DIMENSIONAL LIKELIHOOD RATIO TEST

Generally, it can be assumed that data can be obtained at sample points which are laid out as a rectangular mesh as illustrated in Fig. 1. Our goal is to make a decision on whether there is a mine present at the center location, \mathbf{X} . The data that is available consists of the outputs from the sensor both at the center location and the surrounding locations. Three possible situations can occur:

- (i) there is a mine buried under the center location; or
- (ii) there is nothing buried in this area; or
- (iii) there is clutter located in this area.

The fourth possibility is both a mine and clutter (potentially at different depths) are

present at the location under test. This scenario is treated as situation (i) in this work. Since an EMI sensor is essentially a metal detector, when an object which contains metal is present the sensor will record an induced response due to the object, in addition to background noise. In situation (i), because of the presence of a mine, the sensor response at the surrounding locations may also include a response due to the mine, *i.e.* part of the response may induced by the mine. As the sensor head is moved further and further away from the center point, the effect will vanish. Fig. 2 is a plot of the theoretical prediction of the EM61 sensor response from a metal object with length to diameter aspect ratio of 0.5 at a depth of 0.5 m. The response is plotted over a 2 m by 2 m area. The prediction is obtained using a EMI model based on a dipole approximation of the object (in free space) with the dimension of the Geonics EM61 sensor and with the object parallel to the ground. The overall level of the response shown in Fig. 2 varies depending on the strength of the sensor excitation. For situation (ii), the EMI sensor will only record background noise, and for situation (iii) the response from the position under test might be strong and the response at the surrounding locations might also be disturbed by the clutter response depending on the size and shape of the clutter.

To approach this detection problem statistically, two hypotheses are made. H_1 is the hypothesis that a target (a mine or UXO) is present at the location under test; and H_0 is the hypothesis that a target is not present, *i.e.*, either clutter or background alone is present. In our previous work, a mine/no-mine decision was made by only using data at the single position under test and tested by the (one-dimensional) likelihood ratio detector. The likelihood ratio test for a single sensor response, or location, is defined [15] as:

$$\lambda(r) = \frac{p(r|H_1)}{p(r|H_0)} \underset{H_0}{\overset{H_1}{>}} \beta \quad (6)$$

where r is the received signal from the sensor at the location under test, $p(r|H_1)$ and $p(r|H_0)$ are the probability density functions under the target hypothesis, H_1 , and under the clutter or no-mine hypothesis, H_0 , respectively. When $\lambda(r)$ is greater than the threshold, β , the decision is H_1 . When $\lambda(r)$ is less than β , the decision is H_0 , or no target present. (In the case where $\lambda(r)$ is equal to β , either H_1 or H_0 can be assigned.)

In this work, we have hypothesized that for the land mine and small UXO detection problem the statistics of the sensor response obtained from the locations surrounding a test position may be a function of whether a target is present or not. This dependence will be a function of the target and sensor size, the data sampling grid, *etc.* Based on measured land mine, small UXO and clutter field data from EMI sensors, this hypothesis appears to be valid. Therefore, performance should improve when the information in the neighborhood of the test position is included in the decision process. Hence, we developed a 2-D GLRT detector, which incorporates not only the sensor response at the location under test, but also those obtained from the vicinity of the location under test. A GLRT, as opposed to a LRT, was used since parameters of the probability density functions describing the data are not known exactly and no reliable prior knowledge on these parameters are available. Thus, we chose to estimate the parameters based on training data in order to implement a GLRT.

In [1], [3], we have shown that for a single channel EMI sensor (for instance, the Geonics EM61) the optimum decision statistic at the point by point level is the received signal from the sensor. This decision statistic is equivalent to the one-dimensional LRT, and it can also be shown [17] that for multi-channel EMI data the one-dimensional LRT is equivalent to the 1-D GLRT under some practical assumptions. Hence, fusing data from the 1-D LRT/GLRT at various locations as opposed to using the sensor output or energy level, should result in a further improvement in performance.

Based on the above argument, the input, x , of the 2-D GLRT was chosen to be the output from the one-dimensional LRT at each of the spatial positions. For the single channel time-domain EMI sensor, this is the raw data from the sensor since the single location optimal detector reduces to a threshold test on the raw data as shown in [1], [3]. Since we have assumed that the sensor is subject to Gaussian noise, x is a Gaussian random variable. For the multi-channel EMI sensor, the data considered for the 2-D GLRT is the output of the 1-D GLRT. The 1-D GLRT is a simple version of the 1-D LRT which

avoids extensive computation and provides the same performance to that of the 1-D LRT under a set of assumptions [17]. As defined in [17], the 1-D GLRT is a matched filter-like processor. The output of the 1-D GLRT is the summation of N non-central Chi-square random variables [19] ($N=20$), and thus, can be approximated as a Gaussian random variable based on the Central Limit Theorem.

In the formulation of the 2-D GLRT, two physical properties of the input, x , are explored sequentially. The first property is the spatial change in x across a local area; the second property is the relative size of the center point compared to its neighbors. In fact, this cascade of two generalized likelihood ratio tests is first testing the mine *vs.* background hypothesis, and then testing the mine *vs.* clutter hypothesis.

Because of the small size of the target (between 10 cm and 20 cm) and the sensor dimensions of 1 m (EM61-3D) or 0.5 m (EM61), it was hypothesized that the target would only influence the response at nearby neighbors (within 1 m of the center of a target) [8]. Furthermore, since the input of the 2-D GLRT, x , is the likelihood ratio, its value at a “target present” location will theoretically be larger than those at the neighboring locations which are assumed not to contain targets. Hence, when the center location contains a target, which is often symmetric, the spatial pattern of x will resemble a “peaked” or hill shape, which has maximum value at the center location, and the value decreases from the center in all directions at an approximately equal rate (also see Fig. 2). If there is no metal located at the test area (background only case), the spatial pattern of x will be a spatial Gaussian field (assuming the sensor is subject to white Gaussian noise). For clutter, this spatial pattern will have no predictable pattern; it will depend on the clutter type, shape, size, amount of metal, *etc.* It might appear as a symmetric hill pattern, but can follow other shapes as well (*e.g.* asymmetric). Examples of these patterns from experimental data for target and no-target are shown in Figs. 3 and 4.

The second physical characteristic of a targets is that the absolute value of x for the target is substantially higher than those of its neighbors, and also that of the clutter across

the whole area. For example, a 50 gallon drum will not be considered as a target by the 2-D GLRT detector because even though the spatial pattern somewhat follows a symmetric hill shape, the rate of fall-off of x is not as fast as that for land mines or small UXO across the 2 m by 2 m area.

Therefore, to incorporate the two phenomenologies described above, the 2-D GLRT is formulated as a cascade of two GLRTs, each of which exploits one the two previously described properties. The first GLRT primarily tests situation (i) that is a target buried at the center of the testing area *vs.* situation (ii) that is nothing buried in the testing area, which effectively rejects noise and some of the clutter classes (very small items). The second GLRT tests situation (i) *vs.* situation (iii), which is clutter present case, to eliminate additional clutter whose spatial pattern appears to be a symmetric hill shape. Thus, the 2-D GLRT detector uses a cascade of two GLRTs formulated as follows.

A. Processing Stage 1

The first processing stage exploits the fact that the one-dimensional GLR data within a local area satisfies the symmetric hill pattern when a target is present. In order to achieve this goal, a new variable, \underline{d} , is formed as a vector of the differences between the input x at the center location and those values at the surrounding locations. Based on the sample speed and sensor size during experimental data acquisition, the grid size of data was chosen to be 1m by 0.4m, thus 10 surrounding locations are within 1 m (also the size of bigger sensor, EM61-3D) of the center location, as illustrated in Fig. 5. Hence, the vector of normalized differences from the center location, \underline{d} , is a 10 by 1 vector. Each element of \underline{d} is defined by:

$$d_i = \frac{x_c - x_i}{x_c} = 1 - \frac{x_i}{x_c} \quad (7)$$

where $i = 1, 2, \dots, 10$, x_c is the one-dimensional GLR value at the center location, x_i is the GLR value at i -th location as defined in Fig. 5.

Based on the statistics derived in [1], [3] and the Central Limit Theorem, we have assumed that x is a Gaussian random variable. In [20] and [21], the mathematical form of

the distribution of the ratio of two Gaussian random variables is derived. If $x_1 \sim \mathcal{N}(\mu_1, \sigma_1)$ and $x_2 \sim \mathcal{N}(\mu_2, \sigma_2)$, the correlation coefficient between x_1 and x_2 is ρ , and $v = \frac{x_1}{x_2}$, then the probability density function (pdf) of v is

$$\begin{aligned}
f(v) &= \frac{1}{\pi} \frac{\sigma_1 \sigma_2 \sqrt{1 - \rho^2}}{\sigma_1^2 - 2\rho v \sigma_1 \sigma_2 + v^2 \sigma_2^2} \exp \left[-\frac{1}{2} \frac{1}{1 - \rho^2} \left(\frac{\mu_2^2}{\sigma_2^2} - 2\rho \frac{\mu_1 \mu_2}{\sigma_1 \sigma_2} + \frac{\mu_1^2}{\sigma_1^2} \right) \right] \\
&\quad + \frac{\sigma_1 (\rho \mu_1 \sigma_2 - \mu_2 \sigma_1) + v \sigma_2 (\rho \mu_2 \sigma_1 - \mu_1 \sigma_2)}{\pi (\sigma_1^2 - 2\rho v \sigma_1 \sigma_2 + v^2 \sigma_2^2)^{3/2}} \exp \left[-\frac{1}{2} \frac{(\mu_1 - v \mu_2)^2}{\sigma_1^2 - 2\rho v \sigma_1 \sigma_2 + v^2 \sigma_2^2} \right] \\
&\quad \times \int_0^{\frac{\sigma_1 (\rho \mu_1 \sigma_2 - \mu_2 \sigma_1) + v \sigma_2 (\rho \mu_2 \sigma_1 - \mu_1 \sigma_2)}{\sigma_1 \sigma_2 \{(1 - \rho^2)(\sigma_1^2 - 2\rho v \sigma_1 \sigma_2 + v^2 \sigma_2^2)\}^{1/2}}} \exp \left[-\frac{1}{2} u^2 \right] du
\end{aligned} \tag{8}$$

In this problem, the two random variables (x_c and x_i) are assumed to be independent since noise is independent and identically distributed, thus, $\rho = 0$. Also, the variances of x_c and x_i are assumed to be equal, *i.e.* σ^2 . Therefore, the pdf simplifies to

$$\begin{aligned}
f(v) &= \frac{1}{\pi(1 + v^2)} \exp \left(-\frac{\mu_1^2 + \mu_2^2}{2\sigma^2} \right) + \frac{\mu_2 + \mu_1 v}{\pi \sigma (1 + v^2)^{3/2}} \\
&\quad \times \exp \left[-\frac{(\mu_1 - \mu_2 v)^2}{2\sigma^2(1 + v^2)} \right] \times \int_0^{\frac{\mu_2 + \mu_1 v}{\sigma(1 + v^2)^{1/2}}} \exp \left[-\frac{1}{2} u^2 \right] du
\end{aligned} \tag{9}$$

In [21], the detailed analytical error analysis is provided. Here, we show examples of a comparison of the accurate pdf and Gaussian approximation using estimates of μ_1 , μ_2 and σ that were obtained from the calibration area data. Figs. 6 and 7 provide such comparisons for H_1 and H_0 case, respectively. Clearly, for this problem, a Gaussian approximation to the pdf is acceptable. Thus, we assumed the distribution of \underline{d} is a multivariate Gaussian. Under H_1 :

$$\underline{d}|H_1 \sim \mathcal{N}_{10}(\underline{\mu}_{d_1}, \Sigma_{d_1}) \tag{10}$$

Under H_0 :

$$\underline{d}|H_0 \sim \mathcal{N}_{10}(\underline{\mu}_{d_0}, \Sigma_{d_0}) \tag{11}$$

where \mathcal{N}_{10} represents 10-dimensional Gaussian distribution, $\underline{\mu}_{d_1}$ and $\underline{\mu}_{d_0}$ are the mean vectors, and Σ_{d_1} and Σ_{d_0} are the covariance matrices of \underline{d} under H_1 and H_0 , respectively. The sample means, $\hat{\underline{\mu}}_{d_1}$ and $\hat{\underline{\mu}}_{d_0}$, and the sample covariance matrices, $\hat{\Sigma}_{d_1}$ and $\hat{\Sigma}_{d_0}$, were calculated using the calibration area data (see Sec. IV), and then used as the estimated values of the true means and covariance matrices when calculating GLRs. The elements of the \underline{d} 's are not independent, especially under the H_1 hypothesis. The correlations between the elements are represented by the covariance matrix. This correlation provides an

added incentive to utilize the Gaussian formulation for the GLRT as opposed to assuming independence of the elements of \underline{d} and using Eqn. (9).

Therefore, under these assumptions the decision statistic of the first processing stage has the form:

$$\Omega_1(\underline{d}) = \frac{p(\underline{d}|H_1, \hat{\underline{\mu}}_{d_1}, \hat{\underline{\Sigma}}_{d_1})}{p(\underline{d}|H_0, \hat{\underline{\mu}}_{d_0}, \hat{\underline{\Sigma}}_{d_0})} \quad (12)$$

$$= \frac{\frac{1}{(2\pi)^5 |\hat{\underline{\Sigma}}_{d_1}|^{1/2}} e^{-\frac{1}{2}(\underline{d} - \hat{\underline{\mu}}_{d_1})^T \hat{\underline{\Sigma}}_{d_1}^{-1} (\underline{d} - \hat{\underline{\mu}}_{d_1})}}{\frac{1}{(2\pi)^5 |\hat{\underline{\Sigma}}_{d_0}|^{1/2}} e^{-\frac{1}{2}(\underline{d} - \hat{\underline{\mu}}_{d_0})^T \hat{\underline{\Sigma}}_{d_0}^{-1} (\underline{d} - \hat{\underline{\mu}}_{d_0})}} \quad (13)$$

By taking the logarithm of Eqn. (12) and incorporating the constant terms into the threshold [15], the log generalized likelihood ratio simplifies to:

$$\Omega_1(\underline{d}) = -(\underline{d} - \hat{\underline{\mu}}_{d_1})^T \hat{\underline{\Sigma}}_{d_1}^{-1} (\underline{d} - \hat{\underline{\mu}}_{d_1}) + (\underline{d} - \hat{\underline{\mu}}_{d_0})^T \hat{\underline{\Sigma}}_{d_0}^{-1} (\underline{d} - \hat{\underline{\mu}}_{d_0}) \quad (14)$$

Since a logarithm is a monotonic increasing function, transformation from the original values to logarithmic values does not change the order of the corresponding values, and the resulting performance remains unchanged.

Fig. 8 illustrates the performance of the first processing stage evaluated on synthetic spatial data using the exact pdf of \underline{d} and the Gaussian approximation. Similar performance is achieved when evaluating Ω_1 using Eqn. (12) by substituting the corresponding parameters, or using Eqn. (14), which assumes Gaussian distributed rv's.

B. Processing Stage 2

The generalized likelihood ratio used in the second processing stage is formulated to exploit the second property of the physical nature of the data mentioned above. Another vector, \underline{y} , is formed as:

$$\underline{y} = [x_c \quad \frac{x_c - m(\underline{x}_n)}{x_c}]^T \quad (15)$$

where x_c is the value of the one-dimensional GLR at the center location as before, \underline{x}_n is a 10 by 1 vector which consists of the values of the one-dimensional GLR at the neighborhood locations around the center location as illustrated in Fig. 5, and $m(\underline{x}_n)$ is the

mean value of \underline{x}_n . The first element of \underline{y} is the original x value at the center location. The statistics of x_c partially represent the likelihood of target present at that location since the x 's are obtained from the one-dimensional LR, which is the best decision statistic at the single point by point level. The second element of \underline{y} models the relative size of the center location compared to the locations surrounding it. For targets, this value should be greater than for clutter.

Under the bivariate Gaussian distribution assumption, which was chosen for similar reasons as in the formulation of the generalized likelihood ratio at the first stage, the log generalized likelihood ratio was formulated as:

$$\Omega_2 = -(\underline{y} - \hat{\underline{\mu}}_{y_1})^T \hat{\Sigma}_{y_1}^{-1} (\underline{y} - \hat{\underline{\mu}}_{y_1}) + (\underline{y} - \hat{\underline{\mu}}_{y_0})^T \hat{\Sigma}_{y_0}^{-1} (\underline{y} - \hat{\underline{\mu}}_{y_0}) \quad (16)$$

where $\underline{\mu}_{y_1}$ and $\underline{\mu}_{y_0}$ are the means, and Σ_{y_1} and Σ_{y_0} are the covariance matrices of \underline{y} under H_1 and H_0 , respectively. Again, the estimated values, $\hat{\underline{\mu}}_{y_1}$, $\hat{\underline{\mu}}_{y_0}$, $\hat{\Sigma}_{y_1}$ and $\hat{\Sigma}_{y_0}$, were sample means and sample covariance matrices obtained from the data in the calibration area (see Sec. IV).

C. Cascade of the Two Generalized Likelihood Ratios to Make a Decision

The two generalized likelihood ratios described above exploit the two physical properties of the target and clutter respectively. The overall 2-D GLRT was implemented by cascading the two individual GLRTs by:

- First eliminating the locations at which generalized likelihood ratio 1 is less than its threshold, β_1 .
- Then calculating generalized likelihood ratio 2 for the remaining locations, the final decision is made by comparing generalized likelihood ratio 2 to its threshold, β_2 .

In the first stage, those locations which do not have a symmetric hill pattern indicative of targets are classified as clutter or noise. Then, the second GLRT is applied to further confirm the decision, and the locations which do not satisfy the second statistical model are discarded from H_1 hypothesis. The choice of β_1 and β_2 determines the performance of the detector. If the threshold, β_1 , of GLR 1 is chosen to detect all the targets, *i.e.* set equal

to the minimum value of mine data in calibration area, β_2 will dominate the probability of detection, on the other hand, if β_2 is chosen to detect all mines, P_d will depend on the value of β_1 . The probability of false alarm for the sequential application of both GLRTs is smaller than that of either one of these two GLRTs performed alone. In this analysis, we use the minimum value of GLR 1 corresponding to mine-present hypothesis of each site as the β_1 value, then vary β_2 from its minimum to maximum value to generate an ROC curve. The values of β_1 and β_2 required to achieve the same performance (same P_d and P_{fa}) are different from site to site because the signature for targets at different sites is not the same. This procedure is similar to sensor fusion, the only difference is that here we fuse GLR 1 with GLR 2 only for locations where GLR 1 gives H_1 .

IV. EXPERIMENTAL DETAILS

A. Data

The objective of the *DARPA Background Clutter Data Collection Experiment* [7] was to collect data to aid in the understanding of the effects of clutter on system performance. During the course of the experiment, data was collected using four types of sensors: ground penetrating radar (GPR), electromagnetic induction (EMI), magnetometer, and infrared (IR). Data was collected at four sites distributed over two locations (Fort Carson, Colorado and Fort A. P. Hill, Virginia). The locations represented three different soil types, and exhibited substantial variability in man-made contamination (anthropic clutter). Three of the four sites had a small amount of anthropic clutter, while at one of the sites (Fort A. P. Hill) the amount of such man-made/anthropic clutter was substantial. In addition to the indigenous anthropic clutter, a few synthetic calibration targets, UXO items, and land mines were emplaced at each site.

A typical layout for a test site is illustrated in Fig. 9. The site measured 125 m by 100 m and consisted of three areas: a center square, side bars, and a calibration area. The center square, measuring 100 m by 100 m, was intended primarily for clutter characterization, although 15 calibration targets were placed there to aid equipment calibration and

location registration. Replicas of the calibration targets, along with synthetic unexploded ordnance (UXO) items and land mines were emplaced in the red, blue, yellow, and orange side bars on the sites. A complete description of the targets and their deployment can be found in [7]. In general, the red lane consisted of copies of the registration targets, other targets for calibration, and system-stressing targets. The blue side bar contained UXO and demagnetized spheres, the yellow side bar contained mines, infrared calibration sources, and dielectric targets. The orange side bar consisted of a combination of these, and other targets. The total area of the blue, yellow, and orange side bars was 1300 square meters. The calibration area consisted of a 30 m by 15 m portion of the red, blue, and yellow side bars. Table I lists the metal targets used in the *DARPA* experiments. From these targets and the size of the test sites, one can clearly see the motivation for these experiments was to examine the ability to detect high metal targets and to substantially decrease false alarms through system and algorithm improvements. Data from the calibration area has been extremely valuable in this work since it was used to obtain estimated means and covariance matrices, and to choose thresholds for the 2-D GLRT. The locations and descriptions of the targets in the calibration area (14 of which could be seen by EMI systems) and the center square (10 of which could be seen by EMI systems) were released to the public, the remaining locations (blue, yellow and orange side bars) have not been disclosed. In the analyses that are described below, only data from the calibration areas and the center square are processed to evaluate performance of the various detectors. Clearly, since only 10 targets were emplaced in the 105m x 100m center square, the main goal of these analyses was false alarm rate reduction.

B. Sensors

In this paper, we consider data from two classes of EMI sensors: sensors that integrate time-domain information to provide a single data point (standard metal detector), and those that provide a sampled portion of the time-domain waveform.

The first system, the Geonics EM61, consists of a single-channel pulsed induction system with a 0.5-m transmitter coil positioned approximately 0.3 m above the ground. Data is

received in both the transmitter coil, and a secondary receiver coil that is located 0.4 m above the transmitter. The system operates at a center frequency of 75 Hz; the received signal is integrated from 0.18 to 0.87 ms after each transmit pulse, and the result, a single data point, is stored for later processing. Data were collected along survey lines spaced 0.5 m in the easterly direction, and 0.2 m on the average in the northerly direction.

The second sensor, the Geonics EM61-3D, is a prototype, three-component, time-domain induction system having a 1 m square transmitter coil and three orthogonal 0.5 m receiver coils positioned approximately 0.3 m above the ground. The system operates at a center frequency of 7.5 Hz. Sensor output is measured and recorded at 20 geometrically spaced time gates, spanning a time range from 320 μ s to 32 ms. Data were collected along survey lines spaced 1 m apart in the easterly direction and at a rate of 3 samples per second, or approximately 0.4 m, in the northerly direction.

V. RESULTS

The data used to analyze the detection strategies were collected during the *DARPA Backgrounds Clutter Data Collection Experiment* [7] at four sites at two U.S. locations, Fort Carson, Colorado and Fort A.P. Hill, Virginia. The raw data were first divided into an appropriate raster based on the spatial separation of survey lines and the sampling rate of the sensors, and then all the responses collected in each grid were averaged.

The standard quantitative tool to evaluate performance of a detection algorithm is a receiver operating characteristic (ROC), which is a plot of probability of detection *vs.* probability of false alarm. The performance of each of the detection strategies is shown in terms of an ROC. Figs. 10 and 11 illustrate that the 10-location 2-D GLRT detector operating on the Geonics EM61 sensor data provides a substantial improvement in performance, compared to the standard threshold test at all four sites. In [1], [3], it is shown that the threshold test is the single location optimal detector for the integrated time-domain EMI sensors, thus no separate single location LRT performance is shown.

The improvements of the 2-D GLRT on Geonics EM61-3D sensor data, compared to the standard energy detector, the integral detector, and the one-dimensional GLRT, are demonstrated in Figs. 12 and 13.

Table II lists the actual threshold values used for β_1 for the first processing stage of the 2-D GLRT for all four test sites and two types of sensors. In Tables III and IV, the values of P_{fa} corresponding to P_d equal to 0.95 for various detection approaches are shown. Clearly, the improvement of 2-D GLRT is dramatic. The performance of the δ -technique is also shown in the tables. The decision rule was: if $m \geq 7$, H_1 is true; otherwise, H_0 is true, where m is the number of neighbors which have a smaller energy than that of the center location. The parameter m can be any integer from 1 to 8. Among these values, 8 can provide lowest P_{fa} ; however, the trade-off is that at this value P_d does not usually achieve 100% since there are always some mines which have 1 or 2 neighbors which have higher energy than the center location due to noise. Therefore, 7 was used to obtain the results shown in the tables. It is clear that δ -technique can provide better detection performance than the standard detection methods, but the 2-D GLRT outperforms these alternative detection techniques. The 1-D GLRT performs better than a standard energy or integral test, and an energy detector is generally better than an integral detector. These results are consistent with the theoretical analysis of the performance of these detectors provided in [17].

VI. CONCLUSIONS

The above results indicate that the 2-D GLRT analysis can significantly reduce false alarm rates in land mine and small UXO detection scenarios using EMI sensor data. The performance improvement obtained for both multi-channel time-domain and single channel integrated time-domain EMI data were evaluated at four test sites, and were consistently high across all sites, even at the most highly cluttered Fort A.P. Hill FP20 site. This improvement occurs because the processor may correctly model some of the physical, statistical, and spatial properties of the output of EMI sensors.

Comparing the performance of different time-domain EMI sensors, single channel and multi-channel sensors, the multi-channel sensors provide slightly better performance. Even though the improvement is not significant at this point (because the multi-channel (EM61-3D) EMI is still a prototype sensor under development and the noise level at the receiving coil is high compared to the standard metal detector), it is believed that utilizing a time-domain waveform allows greater exploitation of the phenomenology embedded in the signatures.

For the multi-channel data, an energy detector provides better performance than an integral detector. This can be explained theoretically. At each time gate the noise that receiver is subject to is independent and identically distributed. Therefore, at lower signal levels, the Signal-to-Noise-Ratio (SNR) is less than that at higher signal levels. When applying the same weight to each channel and summing up all channels, (*i.e.* an integral detector), the influence of noise on the low-level signal is highlighted. The energy detector, however, assigns greater weight to the higher-level portions of the signal and less weight to the lower-level portions of the signal (squaring is not a linear, but a quadratic function). Thus, the noise present on the low-level signal will not interfere with the decision as much as it does for the integral detector.

Tables II and III list the performance of different detectors quantitatively. The reduction of P_{fa} for a fixed $P_d = 0.95$ realized by using the 2-D GLRT is at least a factor of 2. For highly cluttered sites, or noisy data, this factor can be as high as 20 over the standard test; a dramatic improvement. This demonstrates that the 2-D GLRT is robust in a noisy environment. The performance of another spatially-based detection strategy, called δ -technique, was also evaluated. This approach is easy to implement and does improve performance over non-spatial algorithms, but the 2-D GLRT provides better performance.

The mean and covariance matrices of the vectors \underline{d} and \underline{y} defined in Sec. II vary across sites. Because close sites provide similar results for the estimated mean and variance, these variations might be caused by the geological differences between the test sites. The

concentration of clutter also affects the variance of the data. To obtain such *a priori* knowledge before remediating an area at a particular site, one solution might be to take a sub-area close to the site as a calibration area to obtain the statistics of this site, then use these statistics to implement a 2-D GLRT. Another solution might be to find the parameters that affect those statistics and apply Bayesian analysis by assuming proper priors to obtain best estimates of those parameters or integrate over all the uncertain parameters.

ACKNOWLEDGMENTS

This research has been supported by the Army Research Office under grant DAAH04-96-1-0448 (Demining MURI). The authors would like to acknowledge the valuable discussions with Dr. Lawrence Carin, Dr. Thomas Altshuler, Ms. Vivian George, Dr. Regina Dugan, Dr. Stacy Tantum, Dr. Erol Gelenbe, and Mr. Taskin Kocak regarding this work. Also, thanks to Dr. Yan Zhang for providing the EMI model code.

REFERENCES

- [1] L. M. Collins, P. Gao, and L. Carin, "An Improved Bayesian Decision Theoretic Approach for Land Mine Detection", IEEE Trans. Geoscience and Remote Sensing, vol. 37 No. 2, March 1998, pp.811-819.
- [2] P. Gao and L. M. Collins, "Improved Signal Processing Approaches for Landmine Detection", Proceedings of SPIE, April 1998, Orlando, FL.
- [3] P. Gao, Improved Approaches to Land Mine Remediation Using Signal Detection and Estimation Theory, Master's Thesis, Duke University, December, 1997.
- [4] G. D. Sower, S. P. Cave, "Detection and Identification of Mines from Natural Magnetic and Electromagnetic Resonances", Proceedings of SPIE, Vol. 2496, Orlando, FL, April 1995.
- [5] N. Geng, P. Garber, L. Collins, L. Carin, D. Hansen, D. Keiswetter, I.J. Won, Wideband Electromagnetic Induction for Metal-Target Identification: Theory, Measurement and Signal Processing, Duke University Technical Report, 1998.
- [6] N. Geng, C. E. Baum, and L. Carin, "On the Low-Frequency Natural Response of Conducting and Permeable Targets", IEEE Trans. Geoscience and Remote Sensing, vol. 37 No. 1, January 1999, pp.347-359.
- [7] V. George, T. Altshuler, A. Andrew, J. Nicoll, E. Cespedes, D. Butler, T. Broach, and R. Mehta, Background Data Collection Plan, DARPA/Defense Science Office, December 1996.
- [8] T. E. Olson and C. E. Priebe, "Detection and Classification of mines via discriminant features and borrowed strength", Proceedings of SPIE, Vol. 3079, Orlando, FL, April 1997.
- [9] C. E. Priebe, "Exploiting stochastic partitions for minefield detection", Proceedings of SPIE, Vol. 3079, Orlando, FL, April 1997.
- [10] I. V. Basawa, "Unilateral Markov random fields for minefield modeling and detection", Proceedings of SPIE, Vol. 3079, Orlando, FL, April 1997.
- [11] E. Gelenbe and T. Kocak, "Area-based results for mine detection", IEEE Trans. Geoscience and Remote Sensing, in press.
- [12] C. E. Baum, Low-Frequency Near-Field Magnetic Scattering from Highly, but Not Perfectly, Conducting Bodies, Phillips Laboratory Interaction Note 499, November 1993.
- [13] Y. Das, J. E. McFee and R. H. Cherry, "Time-domain response of a sphere in the field of a coil: Theory and experiment", IEEE Trans. Geoscience and Remote Sensing, vol. 22, pp.360-367, July 1984.
- [14] Y. Das and J. E. McFee Analysis of an electromagnetic induction detector for real-time location of buried objects, IEEE Trans. Geoscience and Remote Sensing, vol. 28, pp.278-288, May 1990.
- [15] H. L. Van Trees, Detection, Estimation, and Modulation Theory, New York: John Wiley and Sons, 1968. ch. 2, ch. 4. pp.19-116, pp.246-373.
- [16] A. D. Whalen, Detection of Signals in Noise, New York: Academic Press, Inc. 1971. P.352
- [17] P. Gao, and L. M. Collins, "A Theoretical Performance Analysis and Simulation Time-Domain EMI Data for Landmine Detection", submitted to IEEE Trans. Geoscience and Remote Sensing, 1997.
- [18] L. L. Scharf, Statistical Signal Processing: Detection, Estimation, and Time Series Analysis, Massachusetts: Addison-Wesley, 1991. Ch.4, pp.140-149.
- [19] N. L. Johnson, S. Kotz, N. Balakrishnan, Continuous Univariate Distributions, vol.2, 2nd Ed. New York: John Wiley & Sons, Inc, ch.29, pp.433.
- [20] E. C. Fieller, "The Distribution of the Index in a Normal Bivariate Population", Biometrika, **24**, pp.428-440, 1932.

- [21] D. V. Hinkley, "On the Ratio of Two Correlated Normal Random Variables", Biometrika, **56**, pp.635-639, 1969.

LIST OF TABLES

I	Targets emplaced in the center square and the calibration area, where 'Al' means aluminum, 'Fe' means iron and 'AP' mean anti-personnel.	26
II	Threshold values used for the first step process, β_1 , for all four test sites and two types of sensors, EM61 and EM61-3D sensor	27
III	P_{fa} value when $P_d = 0.95$ for EM61 sensor	28
IV	P_{fa} value when $P_d = 0.95$ for EM61-3D sensor	29

Target	Description	Depth to Top (cm)
Fe Sphere	4.875" diameter	5
Al Plate	4" x4" x0.5"	surface
Al Plate	8" x8" x1"	5
Fe Sphere	4.875" diameter	5
Al Plate	4" x4" x0.5"	surface
Al Plate	8" x8" x1"	5
Fe Sphere	4.875" diameter	5
Al Plate	4" x4" x0.5"	surface
Al Plate	8" x8" x1"	5
Fe Sphere	4.875" diameter	5
Al Plate	4" x4" x0.5"	surface
Al Plate	8" x8" x1"	5
Fe Sphere	4.875" diameter	5
Al Plate	4" x4" x0.5"	surface
Al Plate	8" x8" x1"	5
Fe Sphere	4.875" diameter	5
Al Plate	8" x8" x1"	5
Al Plate	4" x4" x0.5"	surface
Al Plate	8" x8" x1"	25
Al Plate	15" x15" x1"	100
Al Spherical Shell	10" diameter	60
Fe Sphere	4.875" diameter	55
Al Plate	white	surface
Al Plate	black	surface
OZM-3	Metal AP landmine	4

Fe Sphere	4.875" diameter	35
81 mm Mortar	UXO	30
152 mm Projectile	UXO	70
155 mm Projectile	UXO	55

TABLE I

TARGETS EMPLACED IN THE CENTER SQUARE AND THE CALIBRATION AREA, WHERE 'AL' MEANS ALUMINUM, 'FE' MEANS IRON AND 'AP' MEAN ANTI-PERSONNEL.

Site	EM61	EM61-3D
FP20	-13.51	-2.23
FP22	-30.64	-3.00
Seabee	-1.08	-17.23
Turkey Creek	-1.70	-3.47

TABLE II

THRESHOLD VALUES USED FOR THE FIRST STEP PROCESS, β_1 , FOR ALL FOUR TEST SITES AND TWO TYPES OF SENSORS, EM61 AND EM61-3D SENSOR

Site	1-D LRT/GLRT	δ -technique ($m \geq 7$)	2-D GLRT
FP20	0.22	0.098	0.016
FP22	0.28	(cannot achieve $P_d=0.95$)	0.059
Seabee	0.066	0.038	0.038
Turkey Creek	0.12	0.048	0.0066

TABLE III

P_{fa} VALUE WHEN $P_d = 0.95$ FOR EM61 SENSOR

Site	Integral Detector	Energy Detector	1-D LRT/ 1-D GLRT	δ -technique ($m \geq 7$)	2-D GLRT
FP20	0.313	0.16	0.125	0.1	0.013
FP22	0.55	0.18	0.27	0.108	0.014
Seabee	0.287	0.099	0.057	0.047	0.016
Turkey Creek	0.158	0.12	0.086	0.059	0.008

TABLE IV

P_{fa} VALUE WHEN $P_d = 0.95$ FOR EM61-3D SENSOR

LIST OF FIGURES

1	Schematic of data placement and data available for a testing location	32
2	Theoretical prediction of EM61 response from a metal object with an aspect ratio of 0.5 at a depth of 0.5m	33
3	Typical spatial response patterns of both mine/UXO and clutter/noise from single channel EMI sensor data	34
4	Typical spatial patterns of both mine/UXO and clutter/noise based on the 1-D GLR of multi-channel EMI sensor data	35
5	The neighborhood locations used when calculating generalized likelihood ratio 1 and 2	36
6	(Top) Probability density functions for the ratio of 2 Gaussian rv's. and a Gaussian approximation for a target present (H_1) case. (Bottom) Error between two pdfs shown in the top figure.	37
7	(Top) Probability density functions for the ratio of 2 Gaussian rv's. and a Gaussian approximation for a target not present (H_0) case. (Bottom) Error between two pdfs shown in the top figure.	38
8	A comparison of performance of the first stage processing using synthetic data based on the exact pdf of d and the Gaussian approximation	39
9	Typical site layout from the <i>DARPA</i> Background Clutter Data Experiment .	40
10	ROC of different detectors based on EM61 data at Fort A.P. Hill FP20 and FP22 sites. The left one, Fig. 10.a, is corresponding to Ft. A.P. Hill FP20 site, the right one, Fig. 10.b, is corresponding to FP22 site. Solid line = 2-D GLRT detector performance, dashed line = performance of standard threshold detector on the received data from EM61 sensor.	41
11	ROC of different detectors based on EM61 data at Fort Carson Seabee and Turkey Creek sites. The left one, Fig. 11.a, is corresponding to Ft. Carson Seabee site, the right one, Fig. 11.b, is corresponding to Turkey Creek site. Solid line = 2-D GLRT detector performance, dashed line = performance of standard threshold detector on the received data from EM61 sensor.	42

- 12 ROC of different detectors based on EM61-3D data at Fort A.P. Hill FP20 and FP22 sites. The left one, Fig. 12.a, is corresponding to Ft. A.P. Hill FP20 site, the right one, Fig. 12.b, is corresponding to FP22 site. Solid line = 2-D GLRT detector performance, dashed line = 1-D GLRT performance, dashed-dotted line = integral detector performance, dash-dot-dot line = energy detector performance. 43
- 13 ROC of different detectors based on EM61-3D data at Fort Carson Turkey Creek and Seabee sites. The left one, Fig. 13.a, is corresponding to Ft. Carson Seabee site, the right one, Fig. 13.b, is corresponding to Turkey Creek site. Solid line = 2-D GLRT detector performance, dashed line = 1-D GLRT performance, dashed-dotted line = integral detector performance, dash-dot-dot line = energy detector performance. 44

N1	N2	N3
N8	X	N4
N7	N6	N5

Fig. 1. Schematic of data placement and data available for a testing location

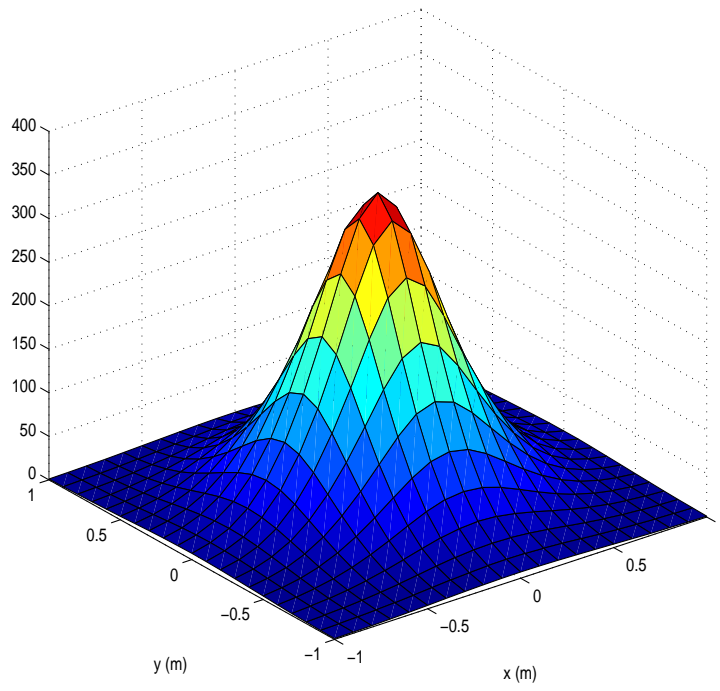


Fig. 2. Theoretical prediction of EM61 response from a metal object with an aspect ratio of 0.5 at a depth of 0.5m

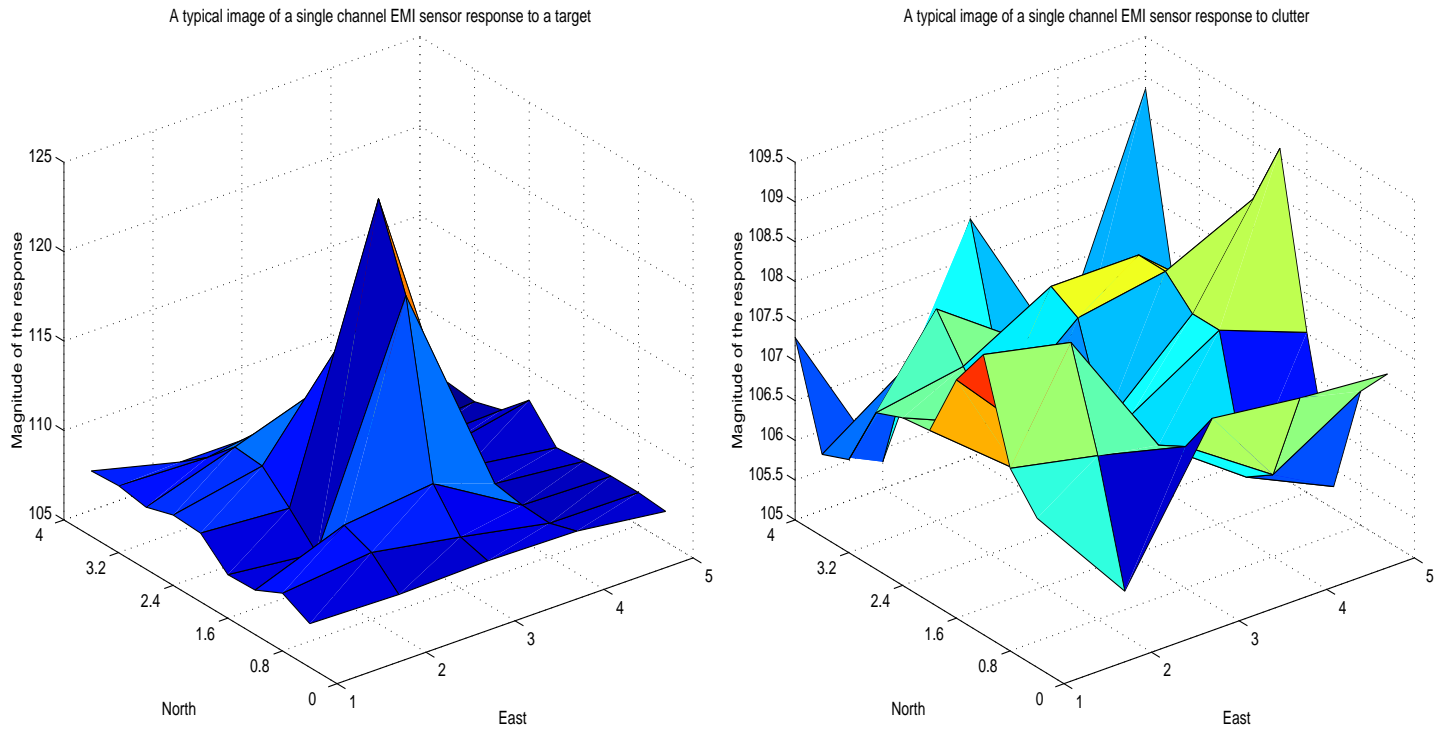


Fig. 3. Typical spatial response patterns of both mine/UXO and clutter/noise from single channel EMI sensor data

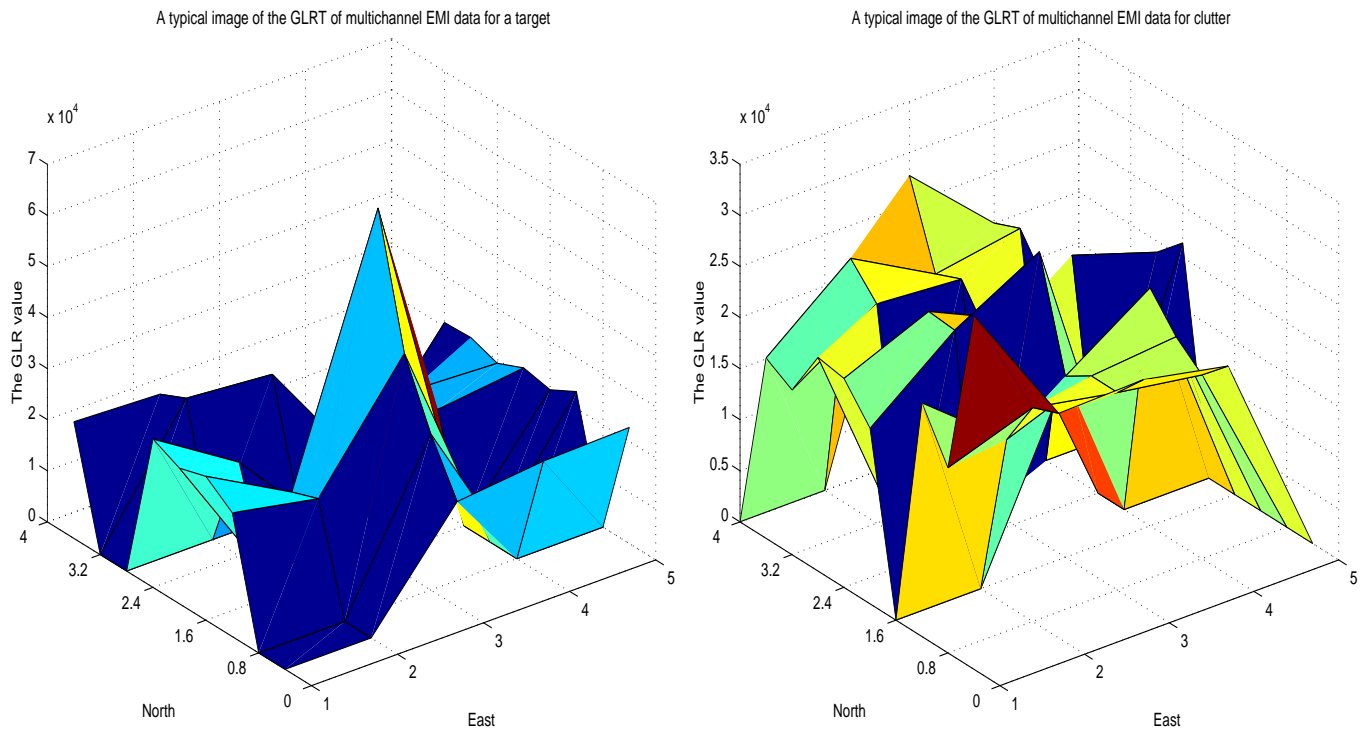


Fig. 4. Typical spatial patterns of both mine/UXO and clutter/noise based on the 1-D GLR of multi-channel EMI sensor data

	X7	
X1	X6	X8
X2	Center	X9
X3	X5	X10
	X4	

Fig. 5. The neighborhood locations used when calculating generalized likelihood ratio 1 and 2

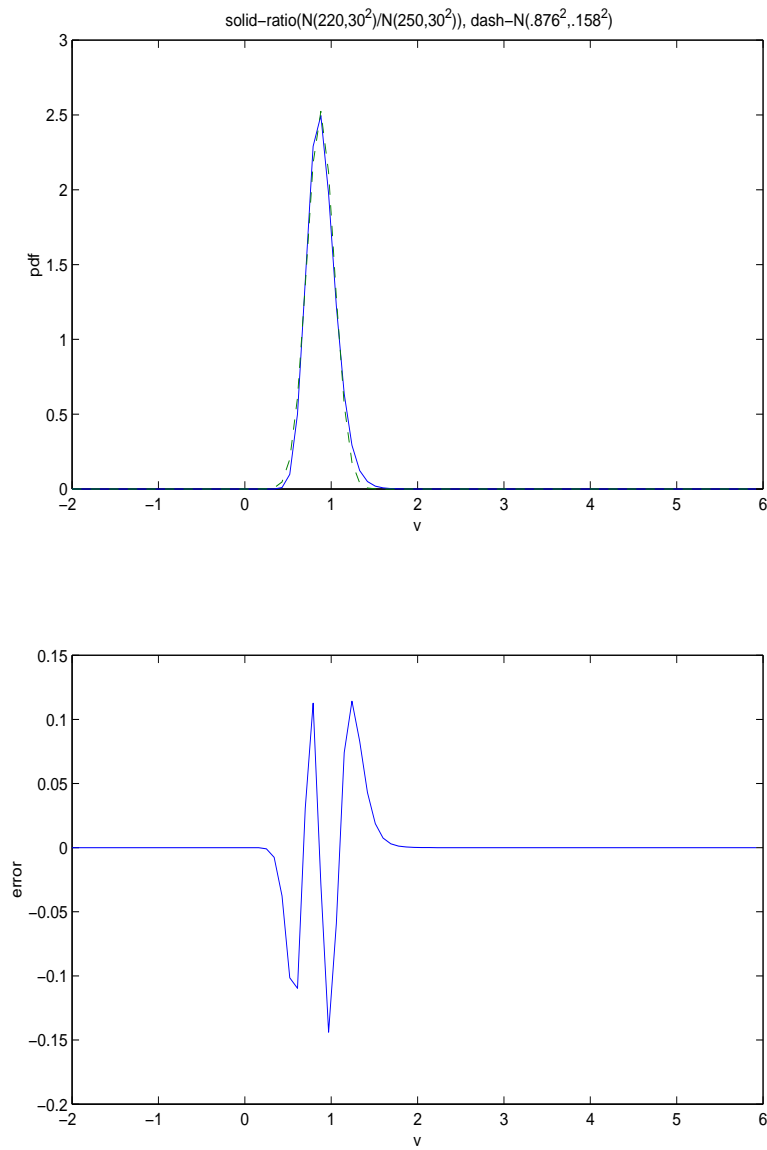


Fig. 6. (Top) Probability density functions for the ratio of 2 Gaussian rv's. and a Gaussian approximation for a target present (H_1) case. (Bottom) Error between two pdfs shown in the top figure.

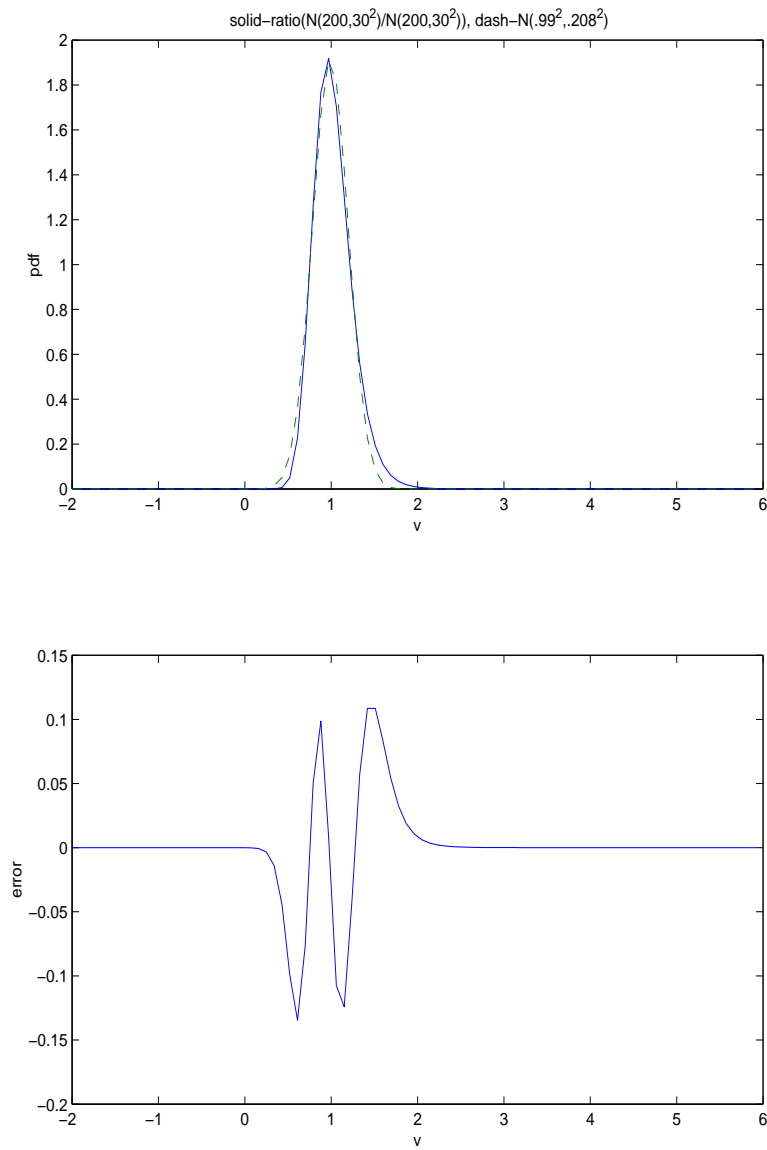


Fig. 7. (Top) Probability density functions for the ratio of 2 Gaussian rv's. and a Gaussian approximation for a target not present (H_0) case. (Bottom) Error between two pdfs shown in the top figure.

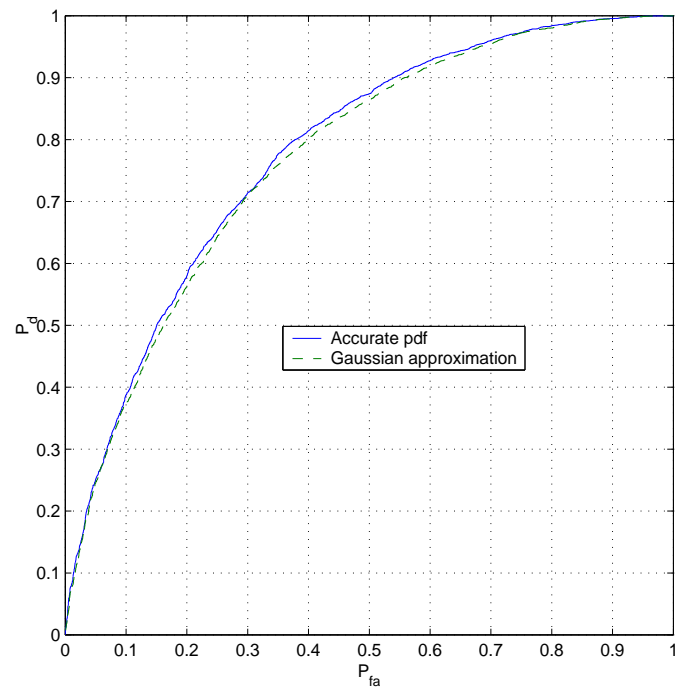


Fig. 8. A comparison of performance of the first stage processing using synthetic data based on the exact pdf of d and the Gaussian approximation

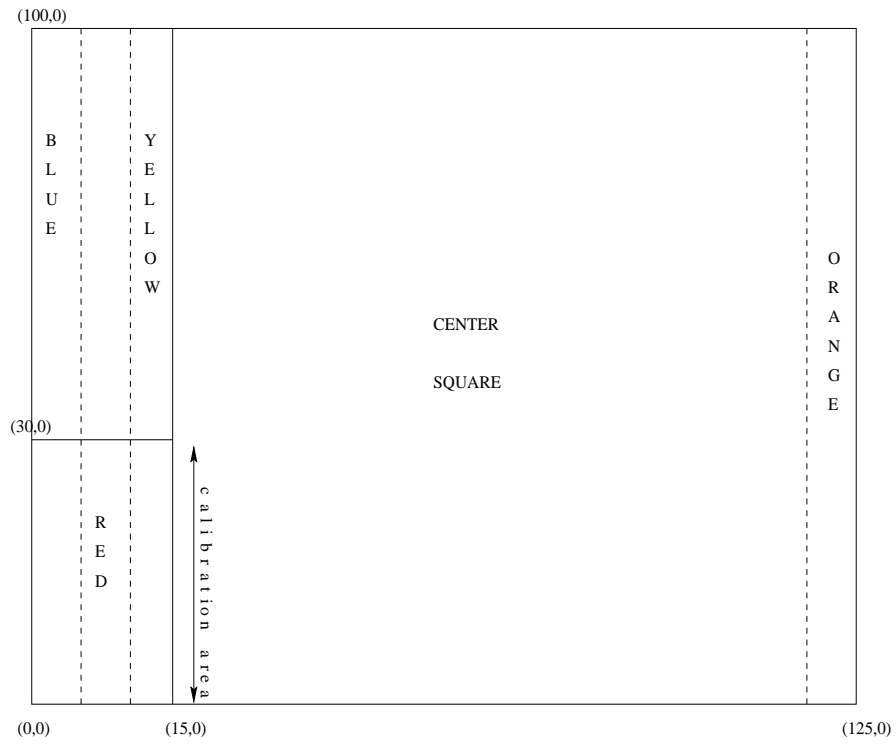


Fig. 9. Typical site layout from the *DARPA* Background Clutter Data Experiment

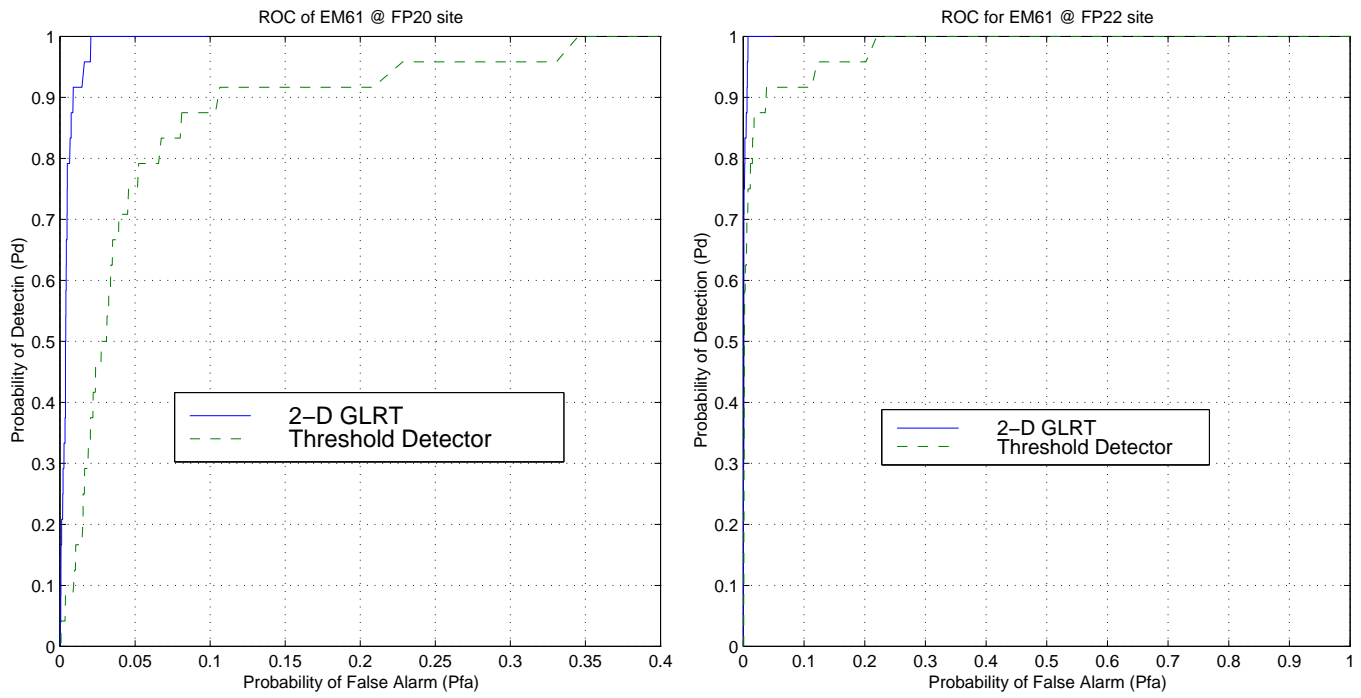


Fig. 10. ROC of different detectors based on EM61 data at Fort A.P. Hill FP20 and FP22 sites. The left one, Fig. 10.a, is corresponding to Ft. A.P. Hill FP20 site, the right one, Fig. 10.b, is corresponding to FP22 site. Solid line = 2-D GLRT detector performance, dashed line = performance of standard threshold detector on the received data from EM61 sensor.

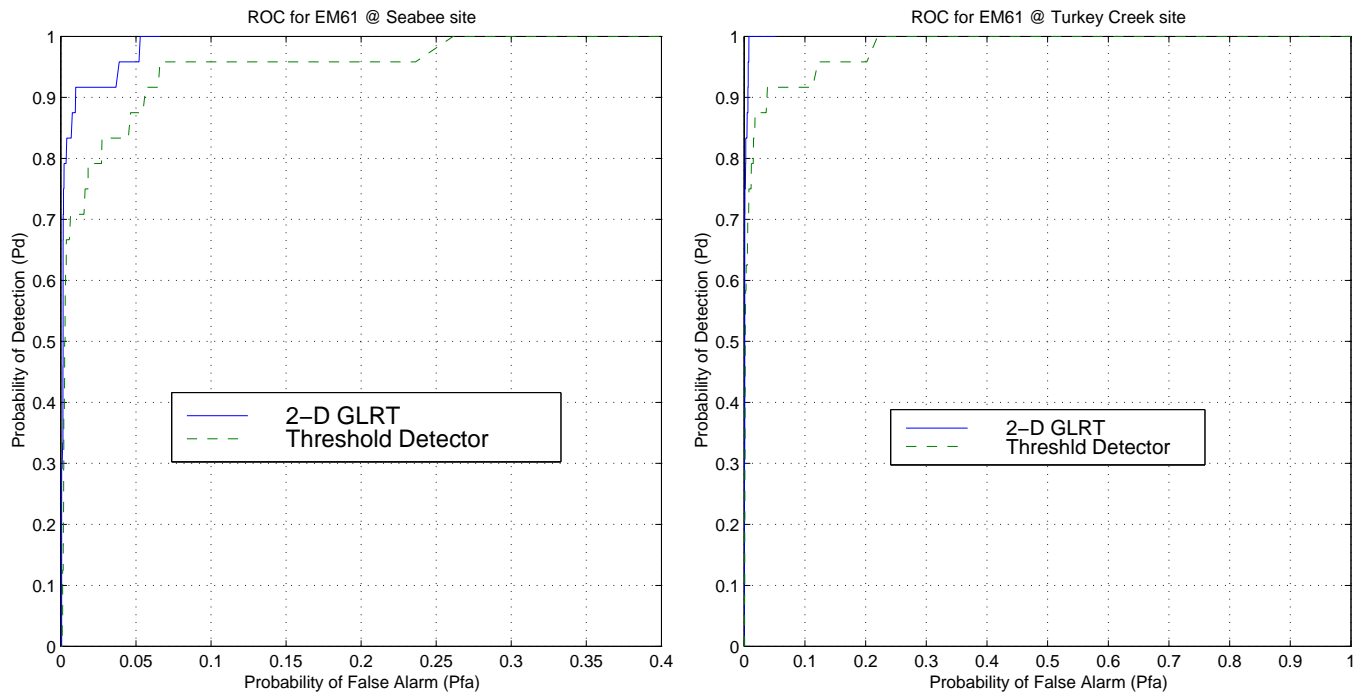


Fig. 11. ROC of different detectors based on EM61 data at Fort Carson Seabee and Turkey Creek sites. The left one, Fig. 11.a, is corresponding to Ft. Carson Seabee site, the right one, Fig. 11.b, is corresponding to Turkey Creek site. Solid line = 2-D GLRT detector performance, dashed line = performance of standard threshold detector on the received data from EM61 sensor.

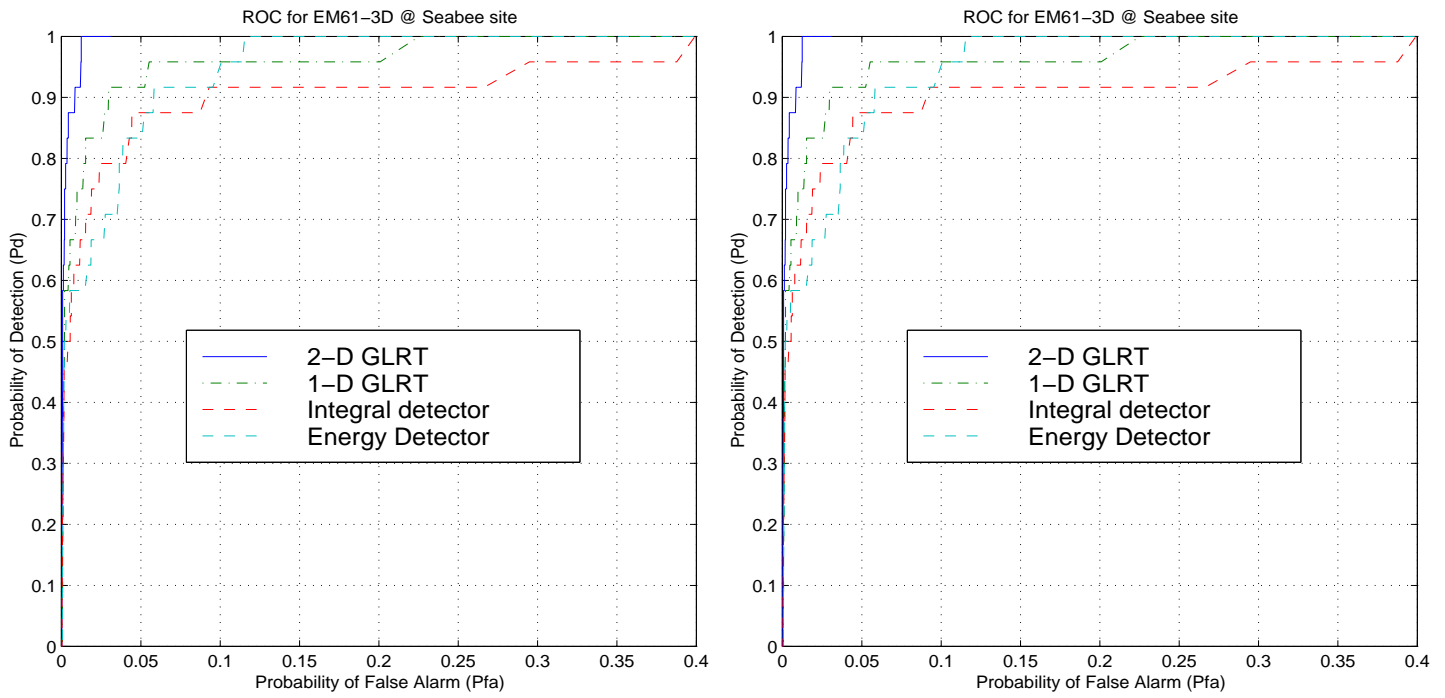


Fig. 12. ROC of different detectors based on EM61-3D data at Fort A.P. Hill FP20 and FP22 sites. The left one, Fig. 12.a, is corresponding to Ft. A.P. Hill FP20 site, the right one, Fig. 12.b, is corresponding to FP22 site. Solid line = 2-D GLRT detector performance, dashed line = 1-D GLRT performance, dashed-dotted line = integral detector performance, dash-dot-dot line = energy detector performance.

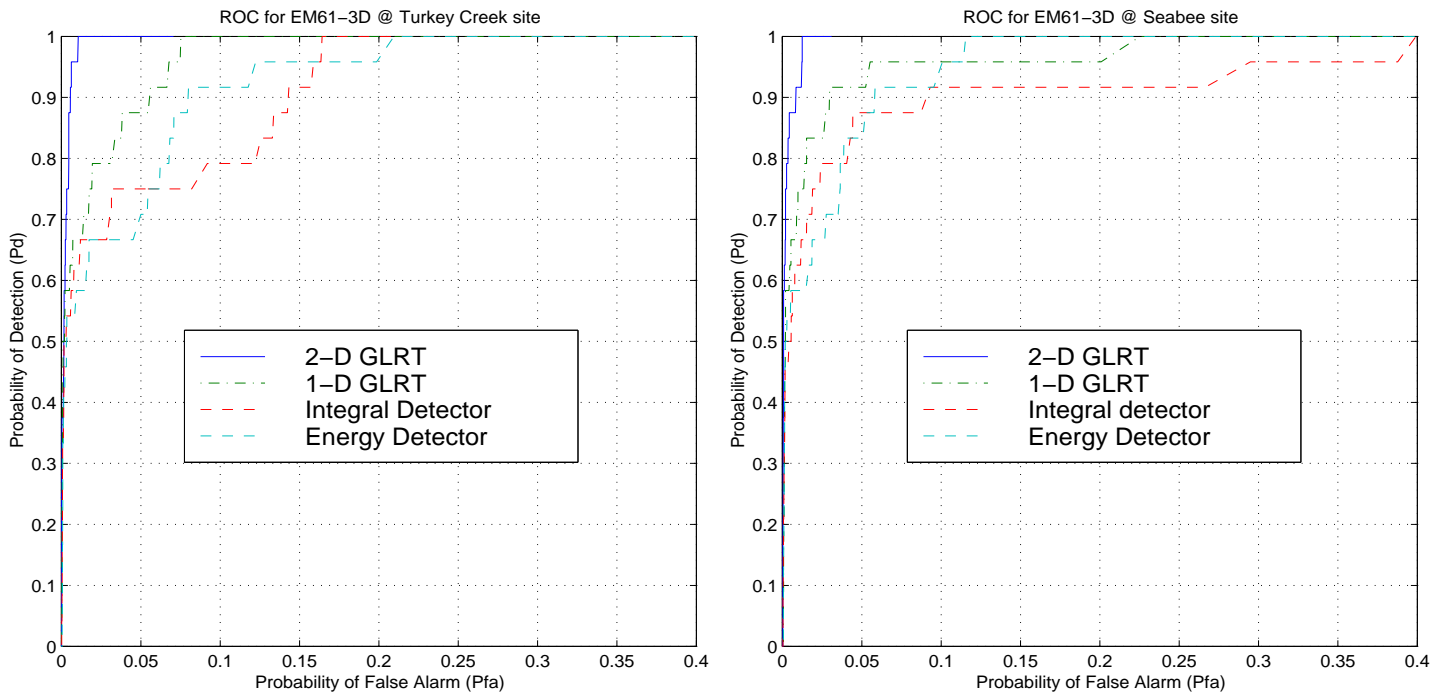


Fig. 13. ROC of different detectors based on EM61-3D data at Fort Carson Turkey Creek and Seabee sites. The left one, Fig. 13.a, is corresponding to Ft. Carson Seabee site, the right one, Fig. 13.b, is corresponding to Turkey Creek site. Solid line = 2-D GLRT detector performance, dashed line = 1-D GLRT performance, dashed-dotted line = integral detector performance, dash-dot-dot line = energy detector performance.